journal

J. Am. Ceram. Soc., **82** [9] 2345–58 (1999)

Aggregation Effects on the Compressive Flow Properties and Drying Behavior of Colloidal Silica Suspensions

J. Jiyou Guo and Jennifer A. Lewis[*]

Department of Materials Science and Engineering and the Beckman Institute for Advanced Science and Technology,
University of Illinois, Urbana, Illinois 61801

The influence of aggregation phenomena on the compressive flow properties and drying behavior of nonaqueous and aqueous silica (SiO_2) suspensions of varying electrolyte (NH_4Cl) concentrations were studied. Compressive rheology measurements, including sedimentation and centrifugal consolidation, were first conducted to investigate consolidation behavior in the absence of solvent evaporation. The volume-fraction-dependent osmotic pressure and compressive yield stress were determined for dispersed and flocculated SiO_2 suspensions, respectively. Consolidation behavior then was studied *in situ* by simultaneously measuring stress evolution and solvent loss as a function of drying time. The observed drying stress histories of the films were complex, consisting of several characteristic regions. First, there was an initial period of stress rise to a maximum drying stress. These measured stress values exhibited good agreement with the osmotic pressure and compressive yield stress at equivalent SiO_2 volume fractions for the dispersed and flocculated systems, respectively. Beyond the maximum drying stress there was a subsequent region of stress decay, which coincided with the draining of liquid-filled pores. No residual drying stress was detected for films prepared from salt-free SiO_2 suspensions, whereas salt-containing films exhibited residual drying stresses likely due to salt-bridging effects. Microstructural characterization of dried films prepared from aqueous SiO_2 suspensions revealed nonuniformities in the spatial distribution of colloidal particles and precipitated salt, with the highest concentrations located at the outer edges of the films. Such features result from capillary-induced transport of these species during drying, and they have important implications on colloidal processing of ceramic thick films and bulk forms.

I. Introduction

Colloidal processing is a mainstay of both commercial and emerging ceramics fabrication routes: examples include pressure filtration,[1–3] osmotic consolidation,[4] gel casting,[5,6] direct coagulation casting,[7] and solid free-form fabrication.[8] Colloidal processing enables one to tailor suspension stability and, hence, control rheological properties and structure evolution (e.g., phase distribution, mass segregation, and pore-size distribution) during processing. However, use of a liquid vehicle is not without difficulties, because it must be removed after shaping. Drying is a critical process step that often leads to problems with dimension control, segregation, and cracking.[9–17] Previous studies on drying have focused on sol–gel films, ceramic films derived from charge-stabilized colloidal suspensions,[10,11,14,15] and tape-cast ceramic layers,[16] with the purpose of relating suspension properties to their structural and stress evolution during drying. Little attention has been given to the influence of aggregation phenomena on the drying behavior of particulate films free of organic binder.

Chiu and Cima[14,15] studied drying of granular films produced from charged-stabilized aqueous α-Al_2O_3 suspensions. First, they determined the critical cracking thickness (CCT), above which such films would spontaneously crack when dried on a rigid substrate. They concluded that the observed cracking phenomena was consistent with a capillary-induced tensile stress acting on the entire film rather than a differential stress generated by a moisture gradient over the film thickness. Furthermore, they identified several processing parameters that affect the cracking behavior of such films. Of these, ceramic particle size, liquid surface tension, and dispersion stability had the most pronounced influence on the CCT of the films. Second, they conducted *in situ* drying stress measurements on films derived from stable dispersions, and they correlated the measured stress to that induced by capillary tension in the liquid phase. However, despite highlighting the importance of suspension stability on cracking phenomena during drying, they neglected to conduct drying stress measurements on films derived from flocculated dispersions.

Here, we investigated the influence of aggregation phenomena on the consolidation behavior of colloidal silica (SiO_2) films produced from aqueous and nonaqueous suspensions of varying stability representative of dispersed, weakly flocculated, and strongly flocculated systems. We first studied their consolidation behavior in the absence of drying via compressive rheology techniques, including sedimentation and centrifugal consolidation. Miller *et al.*[4] recently demonstrated that a strong correlation exists between the consolidation behavior of particle networks under an applied mechanical load (e.g., pressure filtration and centrifugation) and those driven by a chemical potential gradient in the liquid phase of the suspension (e.g., osmotic consolidation). Although equivalent mechanical and osmotic loads did not always result in the same volume fractions, Miller *et al.* observed similar increases in volume fraction with applied driving force, suggesting that both processes are controlled by the force needed to rearrange the particle network. Scherer and coworkers[18] studied the shrinkage behavior of sol–gel-derived ceramics during drying, and they showed that it depends on the magnitude of the capillary drying stress and the rigidity of the gel network. Extending these concepts to drying of particulate films, we then studied the consolidation behavior of colloidal silica films during drying, using the substrate deflection method developed by Chiu and Cima.[15] By comparing the volume-fraction-dependent compressive yield stress with the stress evolution observed *in situ* during drying, we found that the same correlation holds for mechanical and drying-induced consolidation processes. Because no external loads are applied during drying, mechanical equilibrium requires that the capillary tension de-

---

G. W. Scherer—contributing editor

Manuscript No. 190081. Received June 23, 1998; approved February 17, 1999.
Supported by the National Science Foundation under Grant No. DMR 94-53446.

[*] Member, American Ceramic Society.

veloped in the liquid phase exert a compressive force of equal magnitude upon the particle network.[4,18] We quantified this relationship for the first time for colloidal systems of varying suspension stability. We also observed the structural evolution of such films during drying and identified several interesting features that result because of capillary-driven phenomena.

II. Experimental Procedure

(1) Materials System

Monodisperse SiO_2 spheres ($D = 0.5 \pm 0.1$ μm; GelTECH, Alachua, FL) were used as the colloidal phase. The particle density was 2.25 g/cm^3, as measured by helium pycnometry (Model AccuPyc 1330, Micrometrics Instrument Corp., Norcross, GA). The specific surface area, measured by BET (Model ASAP 2400, Micrometrics), was ~4.9 m^2/g, yielding an equivalent spherical diameter of 0.54 μm.

(2) Suspension Preparation

Colloidal suspensions of varying initial SiO_2 volume fraction ($\Phi_s = 0.05$–0.4, depending on the degree of stability) were prepared in deionized water, aqueous NH_4Cl (Aldrich Chemical Co., Milwaukee, WI) solutions with salt concentrations of 0.01*M* or 0.50*M*, and toluene (Aldrich), representing dispersed (0*M* or 0.01*M* salt), weakly flocculated, and strongly flocculated systems, respectively. Upon addition of the appropriate amount of SiO_2, each suspension was stirred for 24 h and intermittently sonicated (Model 550 Sonic Dismembrator, Fisher Scientific, Pittsburgh, PA) every 2 h for a period of 5 min (with a 1 s on/off pulse sequence at 20 kHz). All aqueous suspensions were initially adjusted to pH 5.2. The adjustment of pH was made using stock solutions of analytical-grade NH_4OH and HCl. After the 24 h mixing process, suspension pH was readjusted to 5.2 prior to conducting the experiments detailed below.

(3) Compressive Rheology

Several techniques can be used to measure the compressive flow behavior of ceramic suspensions, including gravitational sedimentation,[19] centrifugation,[4,20–26] pressure filtration,[4] and osmotic consolidation.[4] Here, the first two methods are utilized to quantify the volume-fraction-dependent osmotic pressure ($\Pi(\Phi)$) and compressive yield stress ($P_y(\Phi)$) of dispersed and flocculated SiO_2 suspensions, respectively. In sedimentation, these properties are determined from the equilibrium sediment height as a function of various initial solids loading. In centrifugation, these properties can be assessed by two approaches: (1) measurement of sediment height during centrifugation at multiple spinning speeds,[4,20–23] or (2) measurement of the volume fraction profile during centrifugation[4,23–25] by destructive sectioning[4,23] or by γ-ray densitometry.[24,25]

(A) Sedimentation: As-prepared SiO_2 suspensions of varying solids volume fraction and solution composition were transferred to experimental cells (graduated cylinders of 2.0 cm diameter and 15.0 cm height) to a filled height of 12.8 cm. Each cylinder then was capped to minimize solvent loss during the experiment. The origin of the time scale was taken as the suspensions were poured into the experimental cell. The top interface separating the supernatant and sediment then was recorded as a function of time. $\Pi(\Phi)$ and $P_y(\Phi)$ of the dispersed and flocculated suspensions, respectively, were determined from their final (equilibrium) sediment heights.

(B) Centrifugal Consolidation: As-prepared SiO_2 suspensions of varying solids volume fraction and solution composition were transferred to experimental cells (round bottom tubes of 2.5 cm diameter). Aqueous suspensions were loaded into clear, polycarbon tubes that were partially filled with epoxy to provide a flat bottom necessary for data analysis. These cells were not useful for nonaqueous suspensions because of the dissolution of epoxy in toluene. Hence, nonaqueous suspensions were loaded into clear, Teflon tubes partially filled with white cement to produce the required flat bottom. After curing the cement filler for 200 h in a water-vapor environment, the tubes were pumped in a vacuum desiccator for 24 h to remove residual water. The tubes then were saturated with toluene and finally dried. The amount of toluene intruded into the pores of the cement phase during centrifugation was <1.0%.

Centrifugal loads were applied using a computer-controlled centrifuge (Model Avanti J-25 I, Beckman Instruments, Inc., Schaumburg, IL) equipped with a swing bucket rotor, with varying rotational speeds between 100 and 13 000 rpm. The distance from the center of rotation to the bottom of the suspension in each tube was ~125 mm, providing a maximum acceleration ranging from 4.2×10^2 to 2.3×10^5 m/s^2.

Two approaches were used to determine $P_y(\Phi)$: the multiple-speed and the volume fraction profile techniques.[4] In the multiple-speed technique, $P_y(\Phi)$ was determined from the equilibrium height (H_{eq}) obtained at various spinning speeds. A schematic illustration of the coordinate system for these experiments is given in Fig. 1. Approximately 12 speeds between 200 and 12 000 rpm were chosen, with smaller increments at lower speeds, where the consolidated volume fraction was observed to vary rapidly. After spinning at the desired speed for a prescribed time, the sample was taken out from the centrifuge and the height (H) was measured. This process was repeated until H_{eq} was attained. The speed then was increased and the measurement repeated. H was measured using calipers to a precision of ±0.01 mm. Difficulties occurred when this method was used to measure H_{eq} for dispersed systems. Hence, in the present study, this method was used only for aggregated systems.

The equations governing the network were shown to yield a parametrization in g_0 of the volume fraction and the solids stress at the bottom of the tube, as described by Buscall and White.[20] The pressure ($P(0)$) and the volume fraction ($\Phi(0)$) at the bottom of the tube at each speed were computed using the following equations:[20]

$$P(0,g_0) = \Delta\rho g_0 \Phi_s H_0 (1 - \Delta) \tag{1}$$

where

$$\Delta = \frac{1}{R} \frac{\int_0^{H_{eq}} z\,\Phi(z)\,dz}{\int_0^{H_{eq}} \Phi(z)\,dz} \tag{2}$$

The volume fraction at the base of the cake is given by

$$\Phi(0,g_0) = \frac{\Phi_s H_0 \left(1 - \Delta - \dfrac{\partial \Delta}{\partial g_0}\right)}{\left(H_{eq} + g_0 \dfrac{\partial H_{eq}}{\partial g_0}\right)\left(1 - \dfrac{H_{eq}}{R}\right) + \dfrac{H_{eq}^2}{2R}} \tag{3}$$

The derivative of the height (dH_{eq}/dg_0) at each speed (or acceleration, g_0) was calculated from the fitted curve of H_{eq} as a function of acceleration. The program used to perform

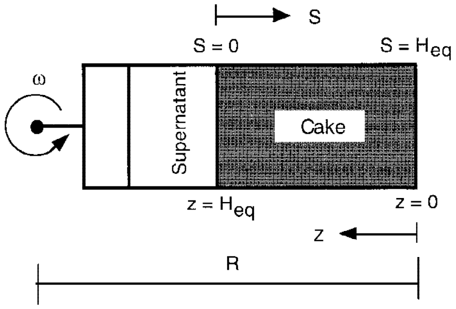

Fig. 1. Schematic illustration of the coordinate systems in centrifugation.

the numerical computation was developed by Zukoski and co-workers.[4]

In the volume fraction profile technique, $P_y(\Phi)$ was determined from the particle distribution of the sediment. At equilibrium, the pressure acting on the particle network at height z in the cake is the accumulated unbouyed weight of the particles above that height, which is a function of distance to the center of the rotor (R). After equilibrium was reached, the volume fraction profile in the sediment cake was determined using a destructive sectioning technique.[4] Slices of the cake above a preselected height in the column were removed from the tube using a specially designed spatula. The diameter of the spatula fitted the inner diameter of the tubes to effectively minimize solvent evaporation during dissection of the cake. A weight-loss technique was used to determine the average volume fraction of each slice (Φ_{ave}). Slices were dried under a $CaSO_4$ desiccant to a constant weight. The yield stress was calculated using the equation[4,19–21,27]

$$P(z) = \int_z^{H_{eq}} \Delta\rho\, g(z)\, \Phi(z)\, dz \tag{4}$$

where z is the height, as measured from the bottom of the suspension, P the pressure acting upon the particle network, $\Delta\rho$ the difference in density between the solid and liquid phases, g the centrifugal acceleration, and Φ the local particle volume fraction.

(4) Drying Behavior

SiO_2 films were cast onto (001) silicon substrates for *in situ* drying stress measurements by placing a known amount of suspension (depending on the desired film thickness after drying) on each surface with a digital micropipette and spreading it to produce a uniform coating thickness. The silicon substrates (Virginia Semiconductor, Fredericksburg, VA) were double-sided, polished (5.08 cm diameter and 50–150 μm thicknesses), and cut into rectangular pieces of 2.54 cm × 2.54 cm. Young's modulus and Poisson's ratio of these substrates were reported to be 1.689×10^{11} Pa and 0.064, respectively. To ensure proper wetting during the suspension coating process, as-received silicon substrates were cleaned using a standard trichloroethane (TCE) cleaning procedure.[17] The substrates were placed in a Teflon carrier and degreased above TCE vapor for ~1 min, then sonicated sequentially (5 min each) in acetone and isopropyl alcohol baths. The substrates were finally rinsed with deionized water, followed by isopropyl alcohol, and then dried in air. After the degreasing procedure, the substrates were placed in a nominally 1.0*M* HF solution for ~2 min to remove the oxidized surface layer.

The experimental apparatus used for *in situ* drying stress and simultaneous solvent loss measurements, shown in Fig. 2(a), was adopted from Ref. 15. Coated substrates were placed immediately on an optical flat, which hung from an analytical balance. Films were dried under ambient conditions. Sample-handling time prior to placement and initiation of data collection was monitored to account for the weight loss that occurred during this brief period. The data correction was most significant (~5% of total weight) for samples of high SiO_2 volume fraction. A monochromatic light source ($\lambda = 0.5461$ μm) was used to generate interference patterns between the reflective back side of the silicon substrate and the optical flat. The evolution of the interference patterns during drying was captured using a video camera. A video frame digitizer was used to chop the desired frames for image analysis after the completion of drying. The radius of curvature (R) of the substrate was determined at a selected time by analyzing the position of fringes in the digitized image, as illustrated in Fig. 2(b).

The average stress in the deposited film is well described by the Stoney equation:[28]

$$\sigma_f = \frac{1}{12Rt_f}\left[\left(\frac{E_f}{1-\nu_f}\right)t_f^3 + \left(\frac{E_s}{1-\nu_s}\right)t_s^3\right]\left(\frac{2}{t_f+t_s}\right) \tag{5a}$$

where E_f, ν_f, and t_f are Young's modulus, Poisson's ratio, and thickness of the deposited film, respectively, and corresponding substrate values are E_s, ν_s, and t_s. Young's modulus of the coating is much less than that of the substrate ($E_f << E_s$); hence, the film stress (σ_f) is, to a good approximation, given by

$$\sigma_f = \frac{E_s t_s^3}{6(1-\nu_s)Rt_f(t_f+t_s)} \tag{5b}$$

with an error <1%–2%.

To determine the CCT of these films, a series of films of varying thickness were cast from each suspension onto 2.5 cm × 2.5 cm glass substrates (~150 μm thickness). These films were dried under the same conditions as those used in stress measurement. The drying process was followed until completion, and then each dried film was examined using optical microscopy (Model BH-2, Olympus Optical Co., Tokyo, Japan) to detect the existence, if any, of cracks. A micrometer (±1 μm) was used to measure the thickness of the dried films. Sixteen measurements were made on each sample, and the average thickness was reported. The average thickness of the thinnest film where local cracking was observed was defined as the CCT.

Film density was determined by a simple geometric method. A profilometer (Model Sloan, Veeco Instruments, Inc., Plainview, NY) was used to determine the thickness of each film for

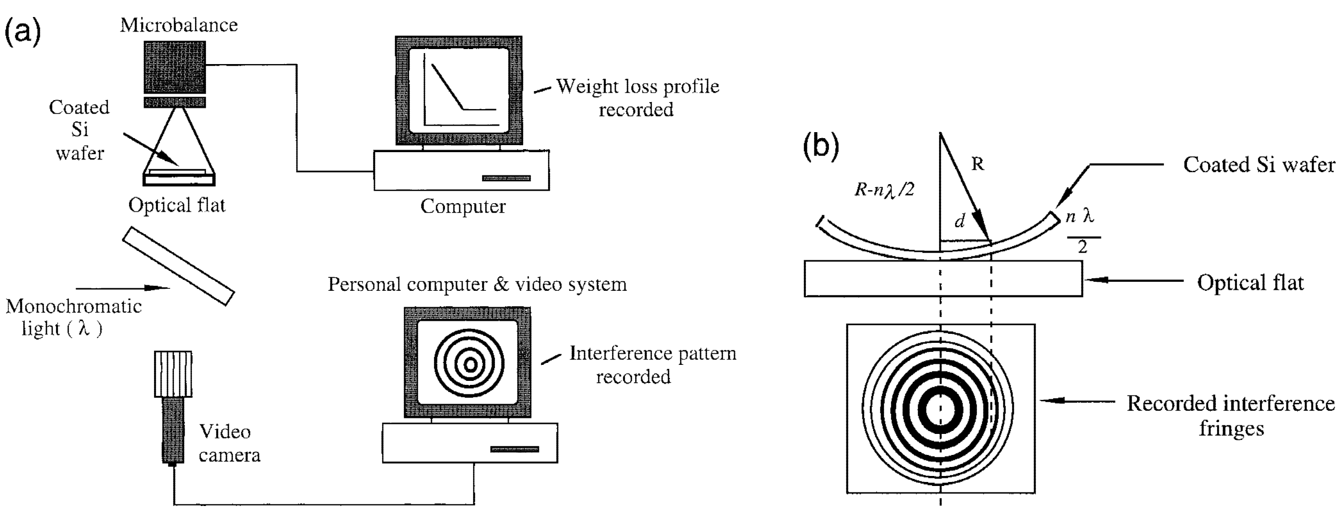

Fig. 2. Schematic illustrations of (a) *in situ* drying-stress and weight-loss measurement apparatus and (b) optical interference pattern analysis.

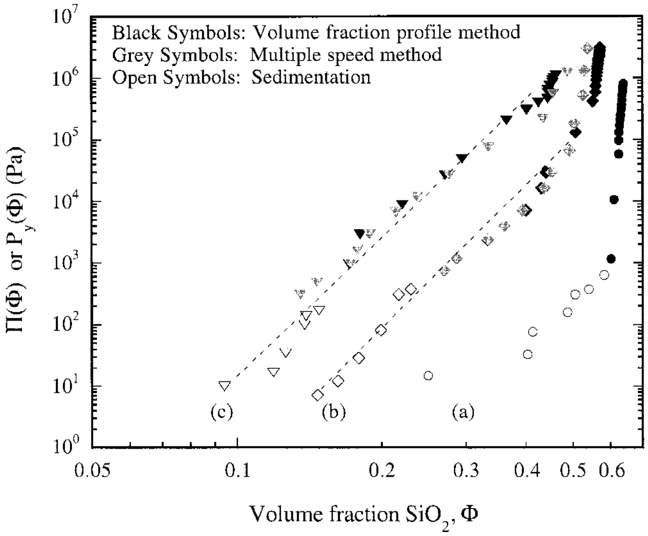

Fig. 3. log–log plot of osmotic pressure and compressive yield stress as a function of solids volume fraction for SiO_2 suspensions of varying solution composition: (a) 0.01*M* NH_4Cl, (b) 0.5*M* NH_4Cl, and (c) toluene.

this calculation. Because of equipment limitations, only those films whose maximum thickness was <100 μm could be measured by this technique. To increase measurement accuracy, films were cut to a 1.0 cm × 1.0 cm square, and the remaining film outside the area was removed mechanically prior to the profilometry measurement. The area of the cut film was determined by image analysis, and its density was determined by dividing its total mass by its volume.

The top surfaces of representative as-dried films were examined by scanning electron microscopy (SEM; Model S-800, Hitachi, Ltd., Tokyo, Japan). A small portion of the dried films was removed mechanically and transferred onto a sample holder with double-sided carbon conductive tape. The samples were then gold-coated and examined by SEM, which was operated at low voltage (5 kV) to minimize surface charging.

III. Results

(1) Compressive Rheological Behavior

A log–log plot of $\Pi(\Phi)$ and $P_y(\Phi)$ as a function of instantaneous volume fraction (Φ) is shown in Fig. 3 for dispersed and flocculated SiO_2 suspensions, respectively. Three data sets were plotted for each system, representing results from sedimentation and centrifugal consolidation via the volume fraction profile and multiple-speed methods. The combination of these techniques allowed the broadest range of instantaneous SiO_2 volume fractions to be probed, with little variation observed between the $P_y(\Phi)$ values obtained from the two centrifugation methods. Dispersed suspensions readily consolidated to a high volume fraction (>0.60) at low pressures (~10^3 Pa). Under the centrifugal loads utilized, the dispersed suspensions produced the most uniform bodies (i.e., narrow Φ distribution). As network strength increased, significantly higher compressive loads were required to consolidate the flocculated suspensions to a given Φ value. For example, compressive loads of 1.49×10^2, 7.51×10^4, and 1.43×10^6 Pa were needed to reach $\Phi = 0.48$ for the dispersed, weakly flocculated, and strongly flocculated suspensions, respectively.

(2) Stress Evolution during Drying

The stress histories and corresponding weight-loss curves for nominally 40 (±1) μm films produced from representative (a) dispersed, (b) weakly flocculated, and (c) strongly flocculated SiO_2 suspensions ($\Phi_s = 0.10$) are shown in Figs. 4 and 5, respectively. The stress histories of such films displayed several characteristic features. First, all films exhibited a period of stress rise (σ_{rise}) during the initial stage of drying followed by a maximum stress (σ_{max}) that coincided with the onset of the saturated state (100% saturation). Following σ_{max}, the average tensile stress in the films decreased as liquid continued to drain from the films (<100% saturation). For films derived from aqueous SiO_2 suspensions that contained salt, the average tensile stress did not relax to zero but, rather, increased in the final stage of drying to a plateau value defined as the residual stress ($\sigma_{residual}$). In contrast, films derived from nonaqueous SiO_2 suspensions fully relaxed upon the completion of drying, and no $\sigma_{residual}$ was detected. Figure 4 reveals the significant differences observed between the magnitudes of the measured drying stresses of such films. For example, σ_{max} values of 0.55, 0.96, and 0.118 MPa were found for films cast from dispersed, weakly flocculated, and strongly flocculated suspensions, respectively. A summary of the drying measurements conducted on all the films as a function of varying initial Φ_s and solution composition is given in Table I. σ_{max} was essentially independent of film thickness studied but exhibited a strong dependence on suspension stability and on initial solids loading (ϕ_S).

The weight-loss curves depicted in Fig. 5 show that the evaporation rate (V_E) remained constant (CRP) during most of

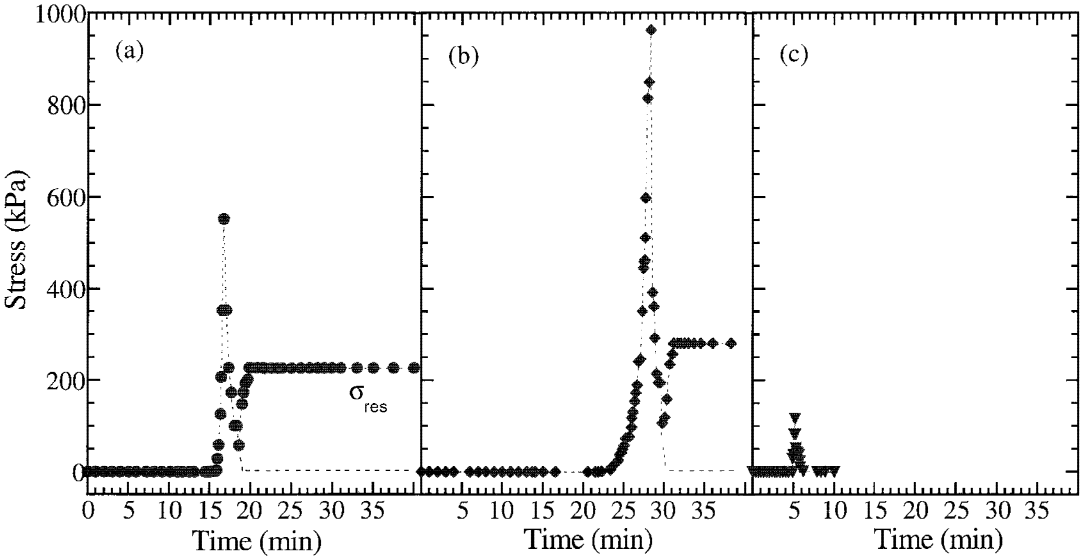

Fig. 4. Drying stress evolution of 40 μm films produced from SiO_2 suspensions ($\Phi_s = 0.10$) of varying solution composition: (a) 0.01*M* NH_4Cl, (b) 0.5*M* NH_4Cl, and (c) toluene.

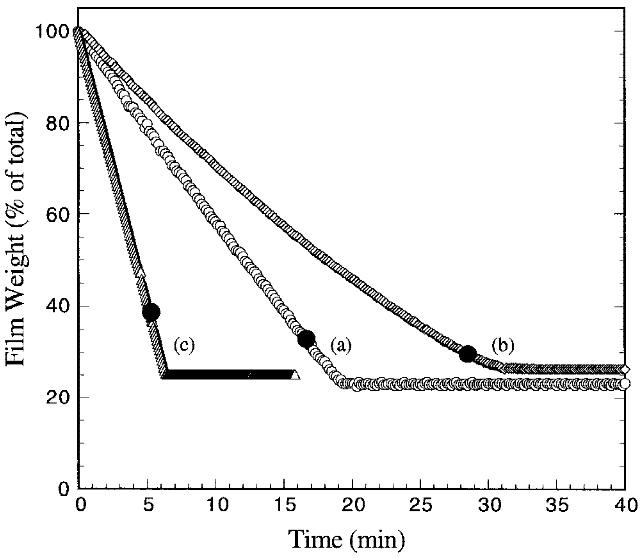

Fig. 5. Weight evolution of 40 μm films produced from SiO_2 suspensions of varying solution composition: (a) 0.01*M* NH_4Cl, (b) 0.5*M* NH_4Cl, and (c) toluene.

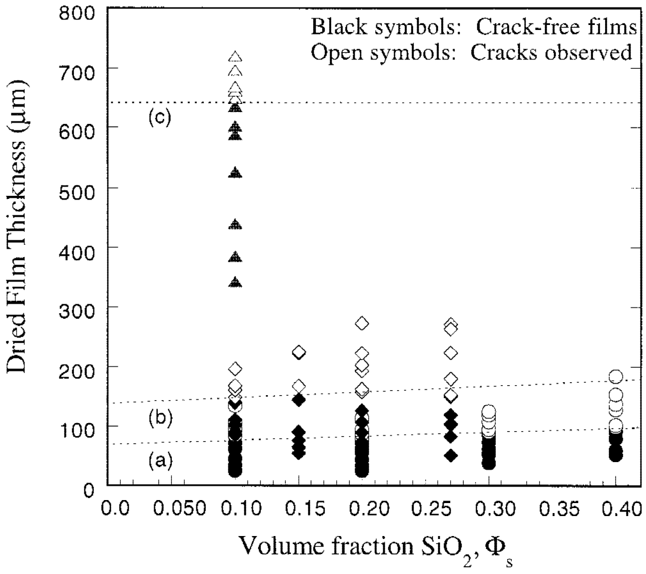

Fig. 6. CCT for films produced from SiO_2 suspensions of varying solution composition: (a) 0.01*M* NH_4Cl, (b) 0.5*M* NH_4Cl, and (c) toluene.

the drying process (>10%–15% saturation) for these films, with the exception of films cast from highly salted, SiO_2 suspensions (0.50*M* NH_4Cl), which exhibited some deviation from constant-rate behavior likely due to the accumulation of dissolved salt species in the liquid near the film surface. As drying proceeded, the salt concentration increase progressively decreased the liquid vapor pressure and ultimately led to precipitation.[29] The solid circle marked on each weight-loss curve denotes the time at which the film reached 100% saturation (Φ_{sat}). As shown in Table I, the time (t_{max}) required to reach σ_{max} decreased with increased Φ_s for a given film thickness, because the amount of solvent loss decreased.

The CCT of films produced from SiO_2 suspensions of varying stability is shown in Fig. 6. The CCT, as denoted by the dashed lines, ranged 80–95, 135–145, and 650–660 μm for films produced from dispersed, weakly flocculated, and strongly flocculated suspensions, respectively. In comparison, SiO_2 films produced from salt-free, dispersed suspensions prepared under analogous pH conditions had a CCT of ~40–50 μm. Hence, modest salt additions (~0.01*M*) led to nearly a twofold increase in CCT because of the formation of salt bridges. Such bridges served as an inorganic binder, thereby strengthening interparticle contacts. The CCT increased moderately with increased initial Φ_s, which was not unexpected, because the total strain (dz/L) the film experienced because of shrinkage in the *z*-direction decreased as Φ_s increased.

(3) Structural Evolution during Drying

Three regions—supersaturated, saturated, and semidry—were identified during drying of SiO_2 films, as illustrated schematically in Fig. 7. The supersaturated region is defined as $\Phi < \Phi_{sat}$, the volume fraction of solids at 100% saturation. In this case, the particle network had either not yet formed or was readily consolidated as further liquid evaporation occurred. The saturated region is defined as $\Phi = \Phi_{sat}$. In this case, consolidation of the particle network ceased and the remaining pore channels were filled with liquid (i.e., 100% saturation). As drying proceeded, the semidry region (<100% saturation) was observed, which was accompanied by the retreat of the liquid/

Table I. Summary of Drying Results for All Films Measured

Solution	Φ_s	Thickness (μm)	t_{max} (min)	Φ_{sat} (±0.03)	Φ_f† (±0.04)	ϕ_{max} (MPa)	ϕ_{res} (MPa)
0.01*M*, pH 5.2	0.10	40.7	16.7	0.62	0.611	0.58	0.25
	0.10	75.0	38.3	0.64	0.611	0.59	0.30
	0.20	44.6	13.2	0.64	0.614	1.20	0.30
	0.20	49.5	14.0	0.63	0.614	1.02	0.35
	0.30	39.2	5.78	0.65	0.660	1.32	0.52
	0.30	56.1	6.90	0.65	0.660	1.27	0.50
	0.40	53.6	3.65	0.64	0.667	1.56	0.75
	0.40	68.1	3.28	0.64	0.667	1.32	0.55
0.5*M*, pH 5.2	0.10	40.0	28.6	0.55	0.550	0.96	0.31
	0.10	60.0	40.5	0.55	0.550	0.90	0.20
	0.15	36.6	11.7	0.56	0.560	1.31	0.25
	0.15	44.9	13.8	0.55	0.560	1.06	0.20
	0.20	39.6	5.73	0.56	0.560	1.16	0.26
	0.20	50.0	6.27	0.56	0.560	1.30	0.25
	0.20	45.3	9.93	0.57	0.560	1.13	‡
	0.27	38.2	2.60	0.57	0.565	1.90	0.25
Toluene	0.10	39.9	5.11	0.45	0.470	0.118	0
	0.10	41.0	5.68	0.46	0.470	0.120	0
	0.10	148	8.13	0.48	0.470	0.112	0

†Data correspond to the average Φ_f at given Φ_s. ‡Uncertain data.

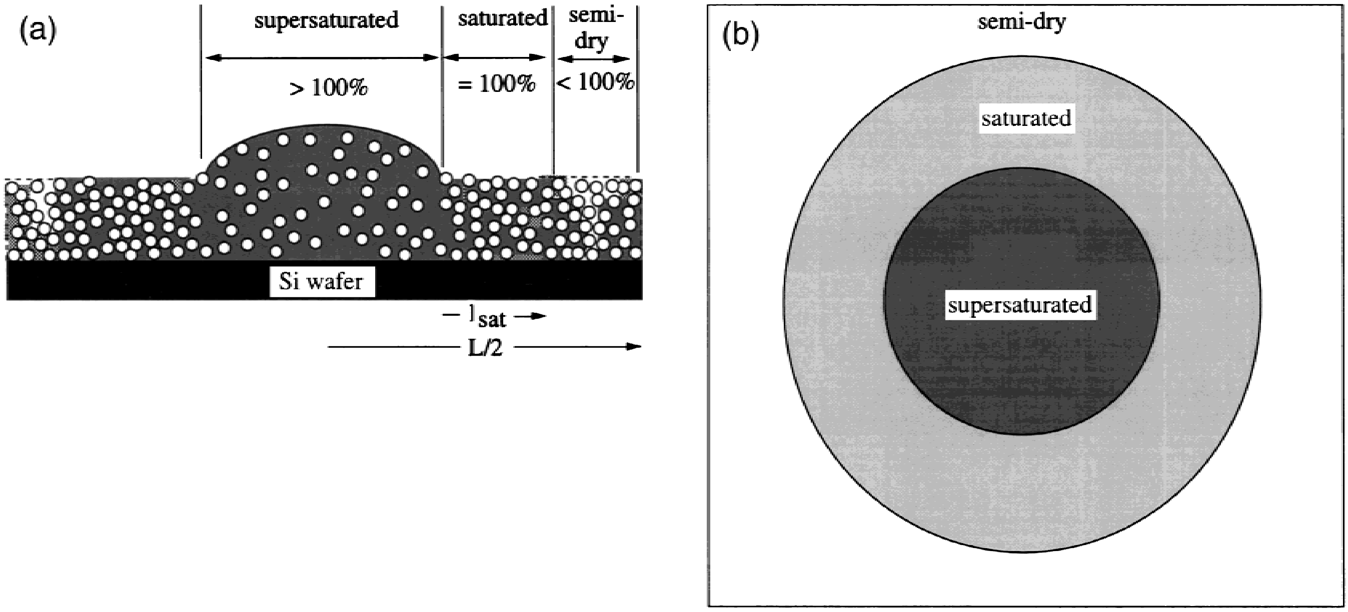

Fig. 7. Schematic illustration of a drying film outlining regions of varying saturation: (a) cross-section and (b) top view.

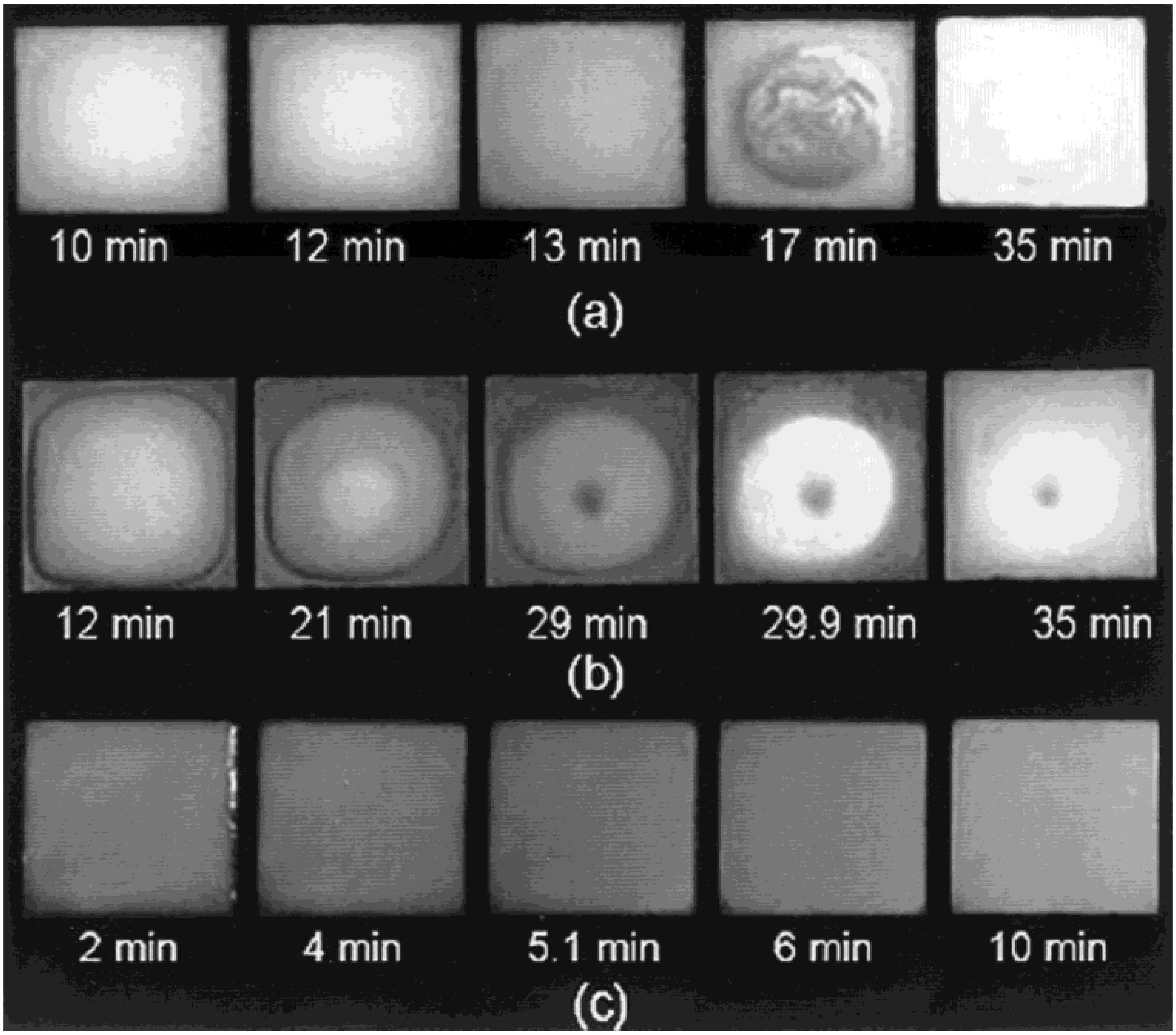

Fig. 8. Optical images of the top surface of 40 μm films produced from SiO_2 suspensions ($\Phi_s = 0.10$) of varying solution composition: (a) 0.01*M* NH_4Cl, (b) 0.5*M* NH_4Cl, and (c) toluene, as a function of drying time. (Film area depicted equals 2.54 cm × 2.54 cm.)

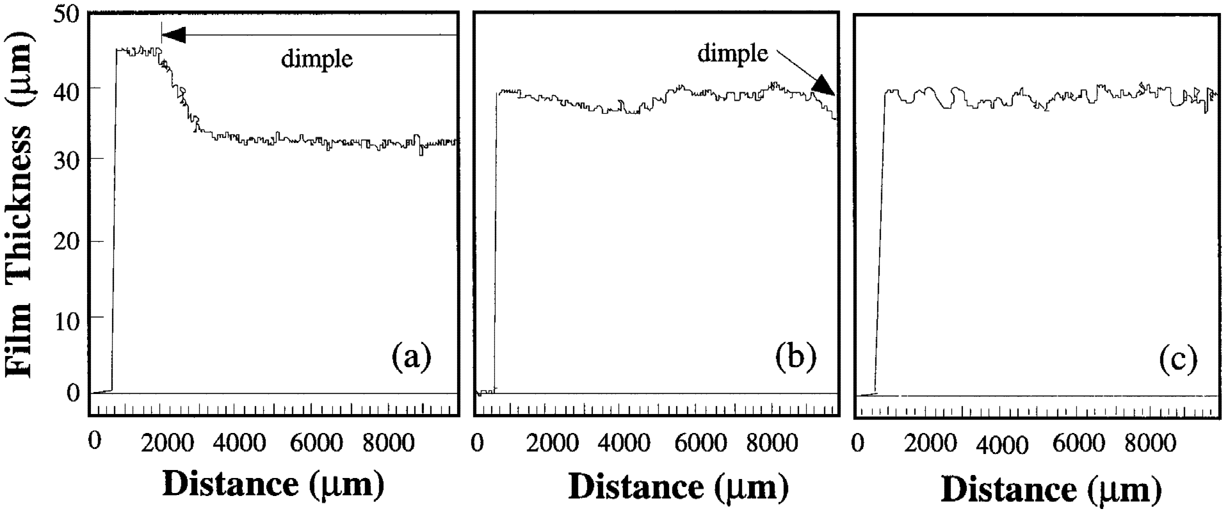

Fig. 9. Film thickness as a function of edge-to-center distance for 40 μm films produced from SiO_2 suspensions ($\Phi_s = 0.10$) of varying solution composition: (a) 0.01*M* NH_4Cl, (b) 0.5*M* NH_4Cl, and (c) toluene.

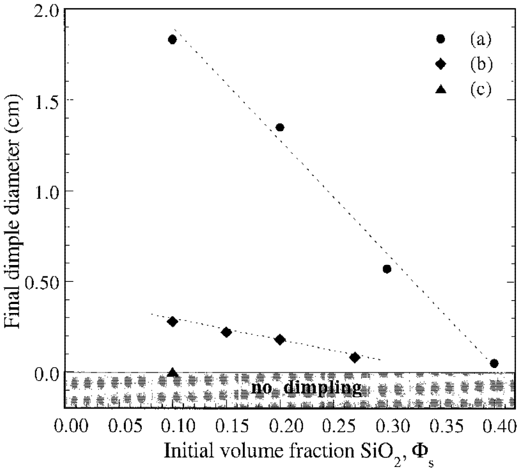

Fig. 10. Characteristic dimple size as a function of initial solids volume fraction for 40 μm films produced from SiO_2 suspensions of varying solution composition: (a) 0.01*M* NH_4Cl, (b) 0.5*M* NH_4Cl, and (c) toluene.

vapor menisci into the film body. In this case, the largest pores connected to the film surface drained preferentially as liquid was drawn to smaller pores of higher suction potential.

Figure 8 shows a series of optical images taken as a function of drying time, in which the top surfaces of representative films produced from (a) dispersed, (b) weakly flocculated, and (c) strongly flocculated SiO_2 suspensions ($\Phi_s = 0.10$) are depicted. The final thickness of each dried film was nominally 40 (±1) μm. Several surface features were observed to evolve as drying proceeded. Films produced from dispersed suspensions dried first along their outer edges, accompanied by an inward shrinkage of the supersaturated region to a finite size. Upon additional solvent loss, this region collapsed, resulting in a depression (or dimple) in the center of the film. Films produced from weakly flocculated suspensions followed the same general trends, except that two saturated regions, defined as outer and inner regions, surrounded the central supersaturated region. The outer region, shaded dark gray, denoted the salt precipitation zone, whereas the inner region, shaded light gray, contained much less salt (refer to Fig. 12 and accompanying discussion). In this case, only a small dimpled region was observed in the center of the film after drying. Finally, films produced from SiO_2 in toluene dried uniformly, such that no boundary between the supersaturated and saturated regions was detected visually. These films collapsed uniformly until the saturated state was reached, and no dimpling was observed.

The characteristic dimple size of each film was evaluated by profilometry. The thickness profiles of representative films are shown in Fig. 9, in which the half-mirror images of their topographical surfaces, as measured from the substrate edge to the film center, are illustrated. This characteristic size is plotted as a function of initial Φ_s in Fig. 10 for several films studied. The extent of dimpling clearly decreased with increased network strength (i.e., fewer "free" particles in suspension) and initial Φ_s (i.e., shorter migration time and decreased $\Delta\Phi$ gradient). The origin of such features as well as their processing implications are addressed in the following section.

SEM photomicrographs of the *center* portion (top surface) of dried films produced from representative (a) dispersed, (b) weakly flocculated, and (c) strongly flocculated SiO_2 suspensions ($\Phi_s = 0.10$) are shown in Fig. 11. Films derived from dispersed suspensions contained close-packed domains (several micrometers in dimension), with a characteristic defect size on the order of the individual particle diameter (refer to Fig. 11(a)). Films derived from weakly flocculated suspensions displayed a less-dense, nonperiodic structure, with a slightly larger characteristic defect size (refer to Fig. 11(b)). There appears to be little evidence of remnant cluster structure, suggesting that capillary-induced structural rearrangement occurred to a significant extent during drying. Finally, films derived from strongly flocculated suspensions displayed the least-dense microstructure (refer to Fig. 11(c)), with the largest characteristic defect size. In this case, remnant clusters were clearly visible, whose size defines that of the defect population.

Figure 12(a) depicts a SEM photomicrograph taken at low magnification of the top surface of a film derived from the weakly flocculated, highly salted SiO_2 suspension (0.5*M* NH_4Cl, $\Phi_s = 0.10$). Three regions, A–C, have been highlighted, progressing inward from the film edge. The diffuse, irregular interface separating the dark- and light-shaded areas corresponds to the boundary between the inner and outer saturated regions observed via optical microscopy during drying (refer to Fig. 8) and appears to be similar in nature to the drying front reported by Shaw.[30] Figures 12(b)–(d) show SEM photomicrographs taken at higher magnification of the highlighted regions A–C, respectively. Large salt precipitates (several micrometers in dimension) decorate the film surface in region A (refer to Fig. 12(b)), masking the underlying particle structure. There also is a small population of particle clusters that reside on top of the salt precipitates. Moving from regions A to C, the population of salt precipitates decreases and the number of visible particles increases.

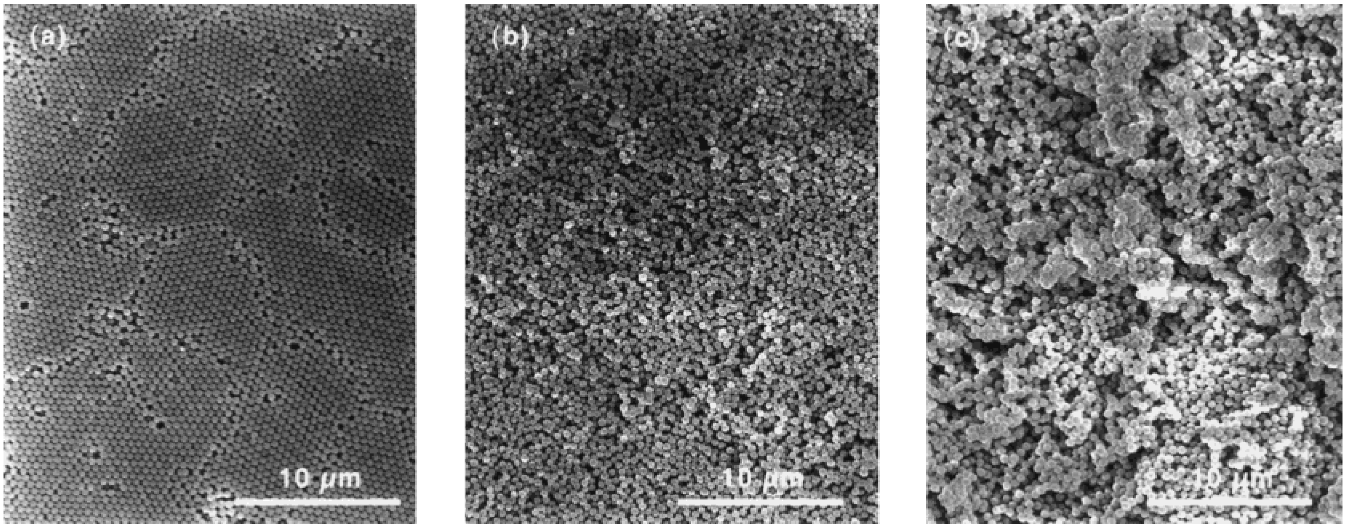

Fig. 11. SEM micrographs of the center region of dried films produced from SiO_2 suspensions ($\Phi_s = 0.10$) of varying solution composition: (a) 0.01*M* NH_4Cl, (b) 0.5*M* NH_4Cl, and (c) toluene.

Energy-dispersive spectrometry (EDS) analysis of identified locations in Fig. 12 yielded the following relative intensities for silicon (Si) and chlorine (Cl) peaks (in at.%) of 56.5 and 43.5 for location 1, 67.1 and 32.9 for location 2, and 90.5 and 9.5 for location 3, respectively. For comparison, EDS analysis of the center region of the film depicted in Fig. 11(b) yielded silicon and chlorine peaks of 99.8 and 0.2 at.%, respectively. Clearly, the salt concentration decreased substantially from the film edge to its center, as reflected by the relative intensities of the silicon and chlorine peaks. Salt precipitation affected the residual drying stress and CCT values for these films, and their microstructural homogeneity.

IV. Discussion

The results clearly show that aggregation phenomena have a significant impact on the compressive rheological properties and drying behavior of colloidal suspensions. In this section, we first examine the measured stress evolution during drying and its relation to the corresponding $\Pi(\Phi)$ or $P_y(\Phi)$ behavior of such suspensions. Next, we discuss the structural evolution of SiO_2 films prepared from systems of varying stability during drying. We begin by addressing the role of capillary-induced structural rearrangement on the consolidation behavior of the particle network. This is followed by an analysis of capillary-driven transport phenomena that lead to structural inhomogeneities (e.g., nonuniformities in film thickness and salt concentration) in the as-dried films. Finally, we discuss the relevance of these observations on colloidal processing of advanced ceramic components.

(1) Drying Stress Evolution

SiO_2 films produced from suspensions of varying stability exhibited remarkable differences in their respective drying stress histories (refer to Fig. 4). Four key regions of behavior were delineated: (1) σ_{rise}, (2) $\sigma_{\max}$, (3) stress decay (σ_{decay}), and (4) σ_{residual}, as illustrated schematically in Fig. 13. During the initial σ_{rise} period, evaporative processes led to an increased Φ_s within the films. Consolidation persisted until the particle network could fully support the drying stress imposed by capillarity. Scherer[10,11] modeled the drying behavior of constrained films undergoing a sol–gel transition. During drying, liquid was transported from the interior to the exterior surface of the films. The tension occurring in the liquid phase induced a corresponding compression of the solid network. Because the drying film adhered strongly to the rigid substrate, its contraction occurred only in the *z*-direction, perpendicular to the film plane (i.e., $\dot{\varepsilon}_x = \dot{\varepsilon}_y = 0$), leading to an in-plane tensile stress in the film.

The average measured stress, σ_{rise}, at any given time is related to the compressive stress imposed on the solid particle network (σ_S) within the film by[10]

$$\sigma_s = \sigma_{\text{rise}}\left(1 - \frac{1-\Phi}{C_\nu}\right) \approx \sigma_{\text{rise}}\frac{4\Phi - 1}{3} \tag{6}$$

where $C_\nu = (1 - 2\nu)/(1 - \nu)$; when $\nu = 0.2$, $C_\nu = 3/4$.

In dispersed systems, the stress transmitted between the particles is defined by the osmotic pressure (Π), which results from repulsive interparticle interactions. Molecular dynamic simulations of hard-sphere suspensions indicate that Π is negligible until the random close-packing limit is approached.[31] Here, we model Π dependence on Φ_s using a modified Carnahan–Starling equation:[32]

$$\Pi(\Phi) = \frac{RT}{\overline{V}}\frac{\Phi(1 + \Phi + \Phi^2 - \Phi^3)}{(\Phi_m - \Phi)^3} \tag{7}$$

where $\overline{V}$ is the molar volume of the particle and Φ_m the volume fraction at maximum close packing.

The $\Pi(\Phi)$ dependence measured by centrifugal consolidation for the representative dispersed system (0.01*M* salt) was well fitted by Eq. (7), yielding $\Phi_m = 0.639$ (i.e., the random close-packed limit). In contrast, significant deviations were observed when attempting to fit these data in the lower Φ range, i.e., the sedimentation results. In this case, Eq. (7) predicted considerably lower values than those observed experimentally.

In flocculated systems, stress is transmitted through a space-filling, aggregated particle network formed when the colloid volume fraction exceeds the gel point (Φ_g; ~0.05).[19] This stress, defined as the compressive yield stress ($P_y(\Phi)$) increases rapidly with Φ.[21,26,27] Previous studies have shown that $P_y(\Phi)$ is well described by a power-law function, when $\Phi > \Phi_g$. Because of the similarity of the flocculated system's mechanical properties at Φ_g, Landman and White[22] have suggested that $P_y(\Phi)$ of flocculated systems of varying network strength should exhibit universal behavior when normalized by their respective Φ_g, as follows:

$$P_y(\Phi) = k\left(\frac{\Phi}{\Phi_g} - 1\right)^n \tag{8}$$

where the gel point varies inversely with the strength of the

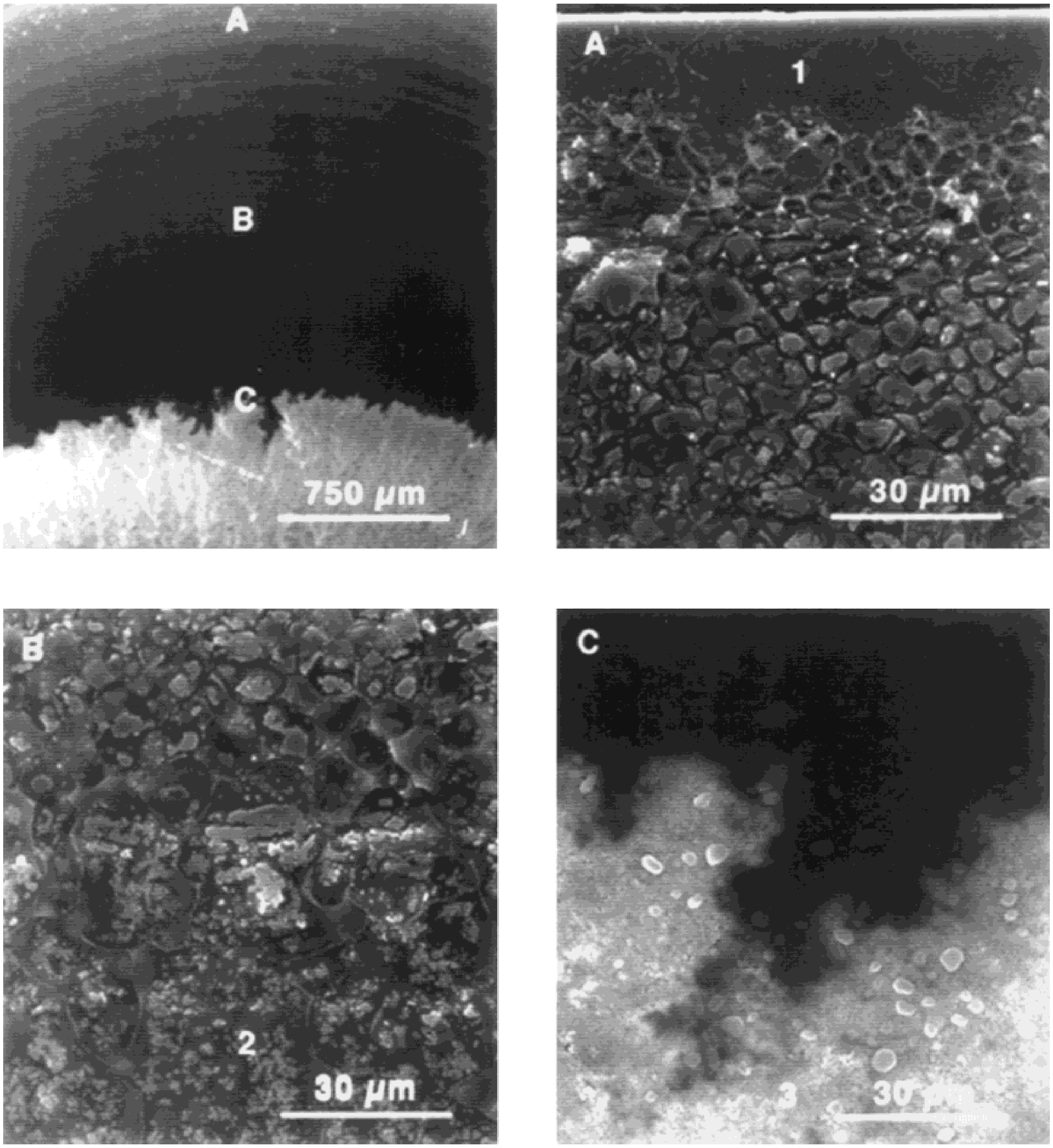

Fig. 12. Series of SEM micrographs at varying magnifications and positions of a dried film produced from a weakly flocculated SiO_2 suspension ($\Phi_s = 0.10$, $0.5M$ NH_4Cl).

interparticle attractions.[19–21,26,27] Using Eq. (8), the scaled $P_y(\Phi)$ behavior for representative flocculated systems (i.e., $0.50M$ salt and toluene) is plotted in Fig. 14. The $P_y(\Phi)$ data form a single, master curve when normalized by the respective Φ_g of 0.045 (for $0.50M$ salt) and of 0.0255 (for toluene), yielding power-law exponents of $n = 6.01$ and $n = 6.67$, respectively. These values of Φ_g, obtained from a best fit of the data, are in excellent agreement with the experimentally determined values of ~0.05 (for $0.50M$ salt) and 0.02 (for toluene) from sedimentation.[33,34]

A comparison of the compressive stress (σ_S) imposed on the solid network during drying to the measured $\Pi(\Phi)$ (dispersed system) or $P_y(\Phi)$ (flocculated systems) behavior is shown in Fig. 15. Although some deviation exists between these data, the general trends convincingly demonstrate the proposed correlation. The origin of the observed deviations likely results from one of two complicating factors: (1) differences in experimental conditions between measurement techniques, and (2) difficulties in accurately assessing $\Phi(t)$ during drying. The first factor is important for aqueous systems that contain salt. During drying, the salt concentration within the films increases as evaporation proceeds, thereby altering the network strength because of diminished electrostatic interactions between colloidal particles as well as salt precipitation effects. In contrast, during compressive rheology, the liquid composition remains constant. Such differences yield a slightly higher drying stress (σ_{rise}) at a given Φ than predicted by compressive rheology experiments. The second factor, although relevant for the aqueous and nonaqueous systems, becomes more significant with increasing solvent volatility. The error associated with estimating $\Phi(t)$ in the drying films is on the order of a few volume percent. However, given, for example, the power-law dependence of $P_y(\Phi)$, even minor deviations in $\Phi(t)$ can lead to large variations between these data.

$\sigma_{\max}$ coincides with the time required for the drying film to reach 100% saturation, i.e., where further network consolidation essentially ceases. Chiu and Cima[15] have studied the drying behavior of films produced from charge-stabilized Al_2O_3

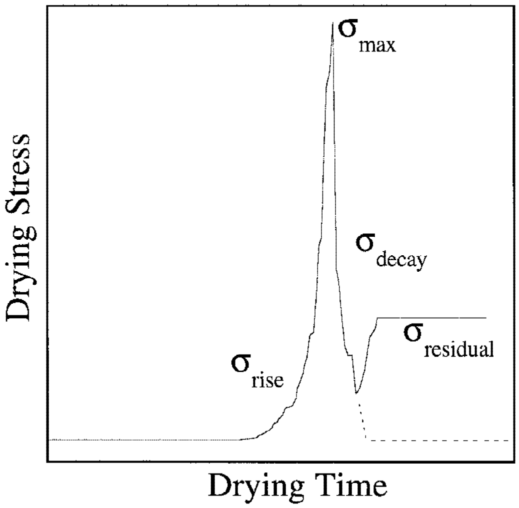

Fig. 13. Schematic illustration of the characteristic drying stress evolution in these SiO_2 films.

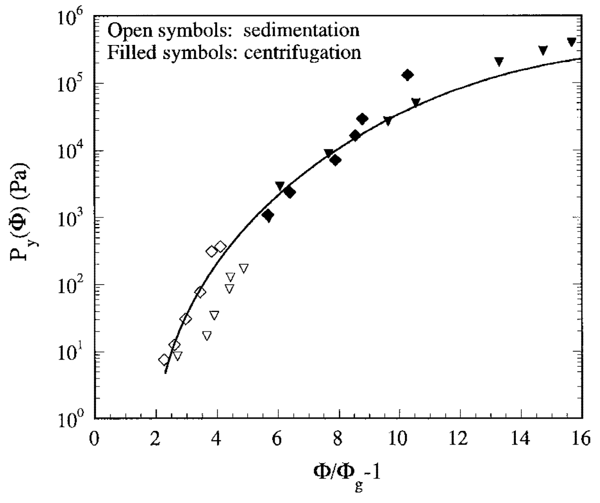

Fig. 14. Semilogarithmic plot of the compressive yield stress versus $\Phi(\Phi_g - 1)$ for suspensions of SiO_2 ((♦) in 0.5*M* NH_4Cl (pH 5.2) and (▼) toluene).

suspensions and have found that σ_{max} is proportional to the surface tension (γ) of the liquid phase and inversely proportional to the particle size. On this basis, they have related σ_{max} to the capillary pressure (P_{cap}) at 100% saturation. P_{cap} in the liquid is given by Laplace's equation:[18]

$$P_{cap} = \frac{2\gamma}{r_p} \qquad (9)$$

where γ is the liquid/vapor surface tension and r_p the characteristic pore size. The liquid/vapor surface tension used is 72 dyne/cm (7.1 Pa) for water (ignoring the effects of dissolved salt species) and 28 dyne/cm (2.8 Pa) for toluene. Assuming that the pore size of the body can be approximated by the hydraulic radius (r_h),[18]

$$r_h = \frac{2\,(1 - \Phi)}{\Phi \rho_s S} \qquad (10)$$

where ρ_s is the theoretical density of the colloidal phase and S the specific surface area. P_{cap} is estimated at 100% saturation to be 1.297, 0.972, and 0.274 MPa for films prepared from dispersed, weakly flocculated, and strongly flocculated SiO_2 sus-

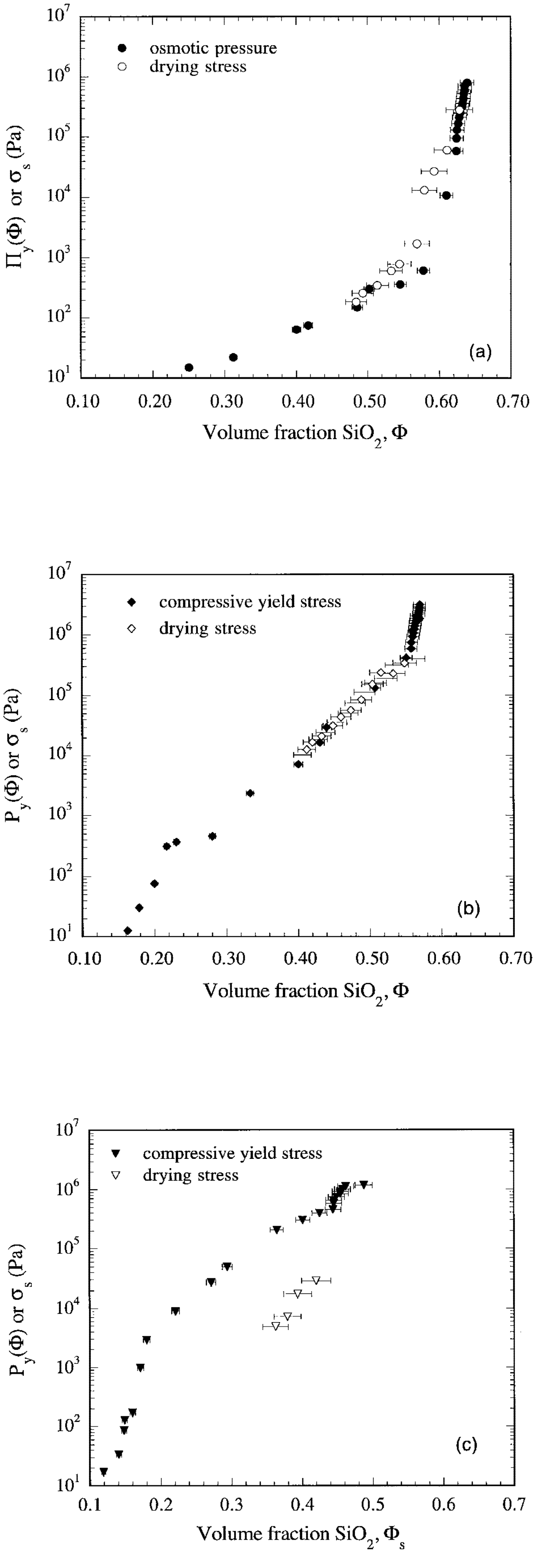

Fig. 15. Semilogarithmic plots of the drying stress and the osmotic pressure or compressive yield stress for SiO_2 suspensions of varying solution composition: (a) 0.01*M* NH_4Cl, (b) 0.5*M* NH_4Cl, and (c) toluene.

Table II. Comparison of σ_{max}, $\Pi(\Phi_{sat})$, and $P_y(\Phi_{sat})$ for SiO_2 Films

Solution	Φ_s	Thickness (μm)	Φ_{sat} ($\pm$0.03)	σ_{max} (MPa)	$\Pi(\Phi)^{\dagger}$ (MPa)	$P_y(\Phi_{sat})^{\dagger}$ (MPa)
0.01*M*, pH 5.2	0.10	40.7	0.62	0.58	0.24–1.10	
	0.10	75.0	0.64	0.59	0.35–1.39	
	0.20	44.6	0.64	1.20	0.35–1.39	
	0.20	49.5	0.63	1.02	0.29–1.12	
	0.30	39.2	0.65	1.32	0.51–1.64	
	0.30	56.1	0.65	1.27	0.51–1.64	
	0.40	53.6	0.64	1.56	0.35–1.39	
	0.40	68.1	0.64	1.32	0.35–1.39	
0.5*M*, pH 5.2	0.10	40.0	0.55	0.96		0.23–1.16
	0.10	60.0	0.55	0.90		0.23–1.16
	0.15	36.6	0.56	1.31		0.25–1.21
	0.15	44.9	0.55	1.06		0.23–1.16
	0.20	39.6	0.56	1.16		0.25–1.21
	0.20	50.0	0.56	1.30		0.25–1.21
	0.20	45.3	0.57	1.13		0.32–1.54
	0.27	38.2	0.57	1.90		0.32–1.54
Toluene	0.10	39.9	0.45	0.118		0.39–0.90
	0.10	41.0	0.46	0.120		0.42–0.98
	0.10	148	0.48	0.112		0.51–1.10

†Represent range for Φ_{sat} of ±0.03.

pensions ($\phi_s = 0.10$), respectively. These values are in reasonable agreement with their respective measured values of σ_{max} of 0.58, 0.96, and 0.12 MPa, particularly given the range of values reported in Table I for systems of varying initial solids loading.

Alternatively, one can relate σ_{max} to the measured properties of the particle network, i.e., its osmotic pressure or compressive yield stress at $\Phi = \Phi_{sat}$. A comparison is presented in Table II, in which a range of $\Pi(\Phi)$ and $P_y(\Phi)$ values are reported based on the accuracy with which Φ_{sat} is known for these films. For films derived from aqueous-based systems, the measured σ_{max} values generally are within the range of $\Pi(\Phi_{sat})$ or $P_y(\Phi_{sat})$ values reported. However, for films derived from the nonaqueous system, the measured σ_{max} values are below the range of reported values. Again, it is recognized that the error associated with estimating Φ_{sat} is greatest for these films, which contain a more volatile solvent.

The period of stress decay following the observed maximum drying stress occurred when liquid menisci retreated into the film body, as the degree of saturation became <100%. For films derived from aqueous-based suspensions, the observed stress did not fully decay to zero prior to undergoing an additional period of rise to some final residual stress value. This transition occurred rather abruptly at ~20.8% saturation (dispersed case) and 28.5% saturation (weakly flocculated case) and was likely associated with local bridging effects resulting from salt precipitation. In contrast, for films derived from nonaqueous suspensions, the observed stress decayed to zero at ~0% saturation.

A period of additional stress rise following the stress decay period was observed for films derived from aqueous-based SiO_2 suspensions. The observed stress approached a steady state (or residual) value in the final stage of drying. This behavior was attributed to the formation of salt bridges, which likely led to an additional (although slight) contraction of the films. Salt precipitation should have occurred when the local concentration of NH_4Cl in solution exceeded 5.5*M*. The estimated values of the salt concentration at the onset of the additional stress rise period for 40 μm SiO_2 films derived from suspensions initially containing 0.01*M* and 0.50*M* NH_4Cl were 0.48*M* and 15.3*M*, respectively, assuming a uniform salt distribution in solution. The large discrepancy in these values was surprising and likely resulted from the known nonuniformity in salt distribution within these films (refer to Fig. 15). Differences in either starting network strength or packing density in the consolidated state also may have contributed to this observed discrepancy. Clearly, a better understanding of the origin of residual stresses and their dependence on local interactions, percolation phenomena, salt concentration, and packing geometry is needed to fully understand these experimental observations.

(2) Structural Evolution during Drying

Capillary-induced structural rearrangement of the solid network during drying has a profound effect on the final microstructure of the as-dried films. The impact of such rearrangement processes is perhaps most readily observed when comparing their extent of consolidation in the absence (i.e., gravity-driven sedimentation) and presence (i.e., drying) of capillarity, as shown in Fig. 16. The magnitude of the error bars depicted in Fig. 16(b) reflects the difficulties encountered in accurately measuring the dried film thickness because of the surface features described earlier.

As expected, films produced from dispersed suspensions yielded higher packing densities than those produced from aggregated suspensions. In both consolidation processes, the packing density exhibited a modest dependence on initial Φ_S. The most dramatic increases in film density between gravity- and capillary-driven consolidation were observed for the flocculated systems. For example, the weakly (0.50*M* salt) and strongly (toluene) flocculated systems settled to maximum volume fractions of ~0.25 and 0.15, respectively. In contrast, under capillary-driven consolidation, these respective systems achieved maximum volume fractions of ~0.55 and 0.45—almost a threefold increase in the latter case. These significant increases in packing density indicated that even strongly aggregated particle clusters could be disrupted and packed more efficiently as drying proceeded (i.e., as the compressive stress on the particle network increased because of increased capillary tension in the liquid phase).

The transport of liquid through a porous medium is governed by the pressure gradient resulting from capillary pressure[11] and obeys Darcy's law, which states that the flux of liquid (J) is proportional to the gradient of pressure in the liquid ($\partial P/\partial x$):

$$J = -\frac{D}{\eta_L}\frac{\partial P}{\partial x} \tag{11}$$

where η_L is the viscosity of the liquid and D the permeability, which is given by[11]

$$D = \frac{(1-\Phi)^3}{5(\Phi S \rho_s)^2} \tag{12}$$

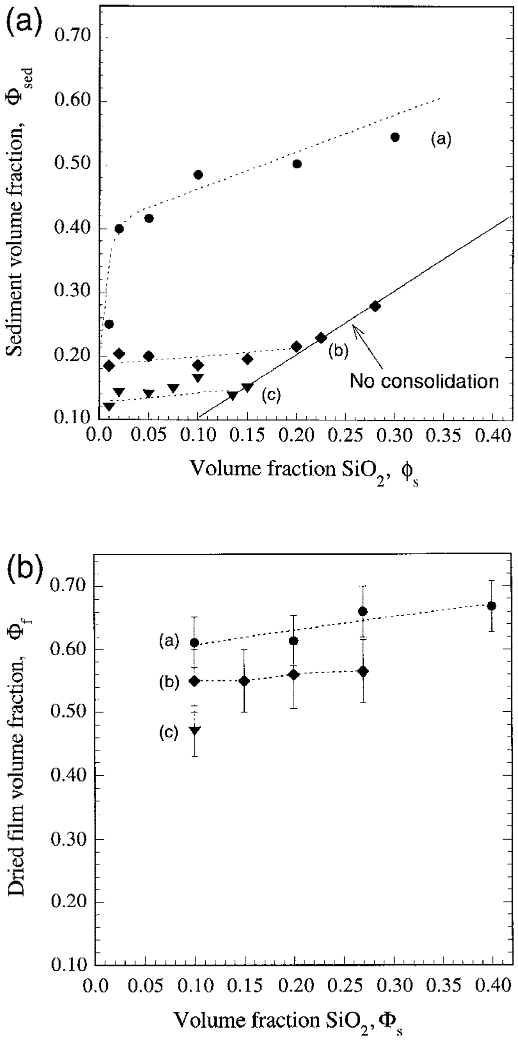

Fig. 16. Comparison of (a) sediment volume fraction and (b) dried-film volume fraction versus initial solids volume fraction upon consolidation of SiO_2 suspensions of varying solution composition: (a) 0.01*M* NH_4Cl, (b) 0.5*M* NH_4Cl, and (c) toluene.

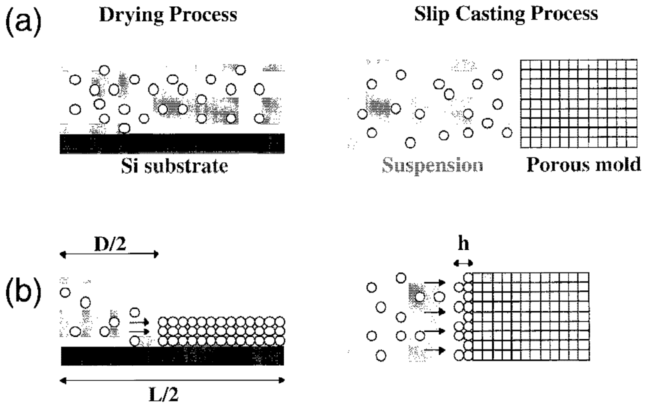

Fig. 17. Schematic illustration of consolidated layer buildup during film drying versus slip casting: (a) initial condition (t = 0) and (b) intermediate condition (t > 0).

where Φ, *S*, and ρ_s have been defined previously. The length scale over which capillary migration occurs during drying has been derived previously:[35]

$$l = \left[\frac{2h(P_s - P_0)(1-\Phi)^3}{5\dot{V}_E\eta_L(S\Phi\rho_s)^2}\right]^{1/2} \tag{13}$$

where P_0 and P_s are the pressures at the boundaries between the supersaturated and saturated regions, and the saturated and semidry regions, respectively. Only SiO_2 films cast from aqueous systems exhibit separately identifiable supersaturated and saturated regions during drying (refer to Figs. 8(a) and (b)). In such films, liquid must be transported from the center (supersaturated) region to the film edge to maintain uniformity in the surrounding saturated regions. Equation (13) provides an estimate of the characteristic length scale for capillary-driven fluid flow. If this length, which corresponds to l_{sat} in Fig. 7(a), exceeds the characteristic film dimensions (i.e., the substrate edge half-length, $L/2$ = 1.27 cm), then saturation uniformity is ensured during the initial stage of drying (>100% saturation). Immediately prior to the disappearance of the supersaturated region, the pressure drop across the saturated region used is P_{cap} at 100% saturation. Given a film thickness of 40 μm, $S = 4.9 \times 10^3$ m²/kg, $\rho_s = 2.254 \times 10^3$ kg/m³, $\dot{V}_E = 1.43 \times 10^{-7}$ m³/(m²·s), and a capillary pressure of 1.297 MPa, this estimated length scale (l_{sat}) is 1.82 cm for films cast from the dispersed suspensions (0.01*M* NH_4Cl). Accounting for differences in their respective evaporation rates, film densities, and P_{cap}, l_{sat} is 1.99 and 0.67 cm for films cast from aqueous (0.50*M* NH_4Cl) and nonaqueous (toluene) suspensions, respectively. For the aqueous systems, these values of the estimated length scale clearly exceed the characteristic sample dimensions, thereby ensuring uniform saturation during drying. In contrast, for the nonaqueous system, l_{sat} is on the order of half the value of $L/2$. However, because of the absence of a localized, supersaturated region (refer to Fig. 8(c)), the appropriate length scale needed to maintain uniform saturation during the initial stage of drying of nonaqueous films is simply on the order of the initial film thickness, ~100 μm.

Several interesting microstructural features (i.e., nonuniformities in the spatial distribution of colloidal particles and precipitated salt) have been observed during the drying of aqueous-based SiO_2 films. Such features result from capillary-induced migration of free colloidal particles and dissolved salt species as liquid is transported from the supersaturated region in the film center to surrounding saturated regions. We begin by considering the first process in greater detail. We hypothesize that dimpling (or alternatively, ring formation) occurs in a manner analogous to slip casting, as illustrated schematically in Fig. 17. As drying proceeds, free particles entrained in the liquid phase migrate to and, ultimately, deposit at the boundary between the supersaturated and saturated regions similar to the deposition that occurs at the suspension–mold interface during slip casting. The height (*h*) of the slip-cast layer and, hence, its mass, exhibits a power-law dependence on time with an exponent *n* of 0.5. If this analogy is valid, then the evolution in ring mass during drying of such films should exhibit this same characteristic time dependence. As an example, ring mass (M_{ring}) versus time is depicted in Fig. 18 for a film cast from a dispersed SiO_2 suspension (ϕ_s = 0.10). M_{ring} is calculated from the following expression:

$$M_{ring} = 0.64\rho_s h_{ring}\frac{L^2 - \pi D^2}{4} \tag{14}$$

where h_{ring} is the right height determined from profilometry (refer to Fig. 9) and D the dimple diameter whose evolution with time has been determined from image analysis (refer to Fig. 8). These data exhibit excellent agreement with expected power-law dependence, as indicated by the slope of 0.5. The extent of dimpling decreases with increasing network strength and increasing initial solids volume fraction in suspension (refer to Fig. 10). These observations can be understood as follows. First, as the network strength increases, the number density of free particles in suspension decreases. Thus, less particle migration occurs during drying. Second, as ϕ_s increases, particle migration is likely suppressed by increasing interactions

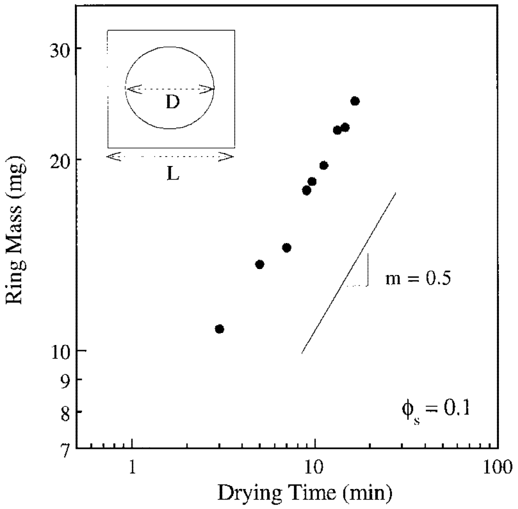

Fig. 18. log–log plot of ring mass as a function of drying time for a 40 μm film prepared from a dispersed SiO_2 suspension ($\Phi_S = 0.10$, $0.01M$ NH_4Cl).

with neighboring particles (i.e., "crowding" effects). Additionally, the timescale for drying decreases, which may also limit the buildup of such features.

Deegan *et al.*[36] have studied related processes, such as printing and coating, and found formation of ring deposits from very dilute, latex suspensions ($\phi \approx 10^{-4}$). They have found that the ring mass also exhibits a power-law time dependence, with a significantly higher power-law exponent, $n = 1.37$. In their analysis, however, Deegan *et al.* have treated the particles only as markers, neglecting their contribution to capillary-driven fluid flow. The significant difference between the observed mass buildup between concentrated and dilute suspensions requires further investigation, given its potential implications on the shape evolution of patterned lines and thick films formed from colloidal systems.

The migration of dissolved salt species during drying is clearly evident in SEM/EDS analysis of the top surface of films cast from salt-containing, aqueous SiO_2 suspensions (refer to Fig. 12). Unlike free colloidal particles, dissolved salt species do not deposit at the boundary between the supersaturated and saturated regions but, rather, migrate to the film surface, where evaporation occurs during the initial stage of drying. As drying proceeds, the pore fluid becomes increasingly enriched in such species. The spatial distribution of precipitated salt on the film surface serves as an excellent tracer to illustrate the direction of fluid flow during drying. Although counterdiffusion of these species must occur along this concentration gradient, transporting species away from the film surface, its mitigating effects are apparently negligible.

(3) Impact on Colloidal Processing

Our findings have several important implications on the colloidal processing of ceramic thick films and bulk forms. We have demonstrated the existence of a strong correlation between the measured stress and structural evolution during drying and the compressive rheological response of the suspended system. To achieve maximum packing density, the $P_y(\Phi)$ behavior should be tailored such that the system can be readily consolidated under the applied processing loads, either external mechanical loads or loads driven by a chemical potential gradient in the liquid phase of the suspension (e.g., drying or osmotic consolidation). Our results further indicate that the final packing density increases with initial solids loading in suspension. On the basis of this observation, it would be interesting to study the effects of relative humidity cycling (e.g., a multistep drying and resaturation process) on the microstructural evolution of such films.

The use of dense, weakly flocculated suspensions has received increasing attention[1–8] because of its many advantages, such as reversible aggregation, minimization of mass-driven segregation and sedimentation, and good consolidation behavior under an applied pressure gradient. We have shown that tailoring the stability of aqueous suspensions through salt additions is not an optimal approach for achieving microstructural homogeneity because of the large variations that result in the spatial distribution of precipitated salt within the dried films. Capillary-driven migration of dissolved species (e.g., salt and organic binder) is expected to occur during drying, provided the size of such species is significantly below the characteristic pore size of the evolving particle network. Local inhomogeneities in the green microstructure would likely persist in the final, sintered body, resulting in decreased component reliability. Thus, although salt precipitation strengthens the particle network, thereby increasing the CCT of these films, its incorporation as a processing aid in the initial suspension formulation should be avoided if possible. An alternate means of tailoring suspension stability in this case would be to adsorb short-chain, steric additives onto the ceramic particle surfaces and handle the suspensions near their isoelectric point to mitigate electrostatic contributions. As a result of the above discussion, the purpose would be to develop a very weak attractive interaction energy (i.e., a secondary well depth on the order of ~KT) by incompletely compensating the long-range van der Waals interactions between particles. Additional studies are needed to ascertain the desired conformation and coverage of such stabilizing species so that maximum interparticle lubricity is achieved.

Finally, we have shown that the shape evolution of particulate films during drying can lead to interesting microstructural features, such as dimple (or ring) formation. Such observations are perhaps most relevant for emerging solid free form (SFF) fabrication routes that involve layer-by-layer deposition of colloidal suspensions. In this approach, line definition is critically important, because it defines the minimum feature size within the as-formed bodies. To minimize complications resulting from capillary-driven particle migration during drying of such geometries, it is desirable to process dense, flocculated suspensions in which the presence of free particles is negligible. In some cases, it may be desirable to deposit multiple lines in a single deposition step, whose resolution exceeds that of the characteristic print diameter. In this situation, the tendency toward ring formation can be exploited by processing dilute, dispersed suspensions in which particles are entrained during drying and deposit at the line edges.

V. Summary

The influence of aggregation phenomena on the compressive rheological properties and drying behavior of aqueous SiO_2 suspensions with varying electrolyte (NH_4Cl) and nonaqueous (toluene) concentrations has been studied for the first time. Sedimentation, centrifugal consolidation, *in situ* drying stress measurements, and microstructural analysis have revealed that aggregation phenomena significantly impact volume-fraction-dependent osmotic pressure or compressive yield stress behavior, drying stress histories, and structural evolution during consolidation. Several interesting features, including salt segregation and surface dimpling, have been observed in as-dried films prepared from aqueous systems. Such features result from capillary-induced transport of free particles and dissolved salt species. The formation of a dimpled region (or, alternatively, a solid ridge around the outer film edge) is analogous to the slip-casting process. Finally, the ramifications of our observations on colloidal processing of advanced ceramics were discussed.

Acknowledgments: The authors wish to thank C. Zukoski for many fruitful discussions of this work and S. Morissette and C. Martinez for assistance during this work.

References

[1] J. C. Chang, F. F. Lange, and D. S. Pearson, "Pressure Sensitivity for Particle Packing of Aqueous Al_2O_3 Slurries vs Interparticle Potential," *J. Am. Ceram. Soc.*, **77** [5] 1357–60 (1994).

[2] B. V. Velamakanni, F. F.Lange, F. W. Zok, and D. S. Pearson, "Influence of Interparticle Forces on the Rheological Behavior of Pressure-Consolidated Alumina Particle Slurries," *J. Am. Ceram. Soc.*, **77** [1] 216–20 (1994).

[3] J. C. Chang, F. F. Lange, and D. S. Pearson, "Viscosity and Yield Stress of Al_2O_3 Slurries Containing Large Concentrations of Electrolyte," *J. Am. Ceram. Soc.*, **77** [1] 19–26 (1994).

[4] K. T. Miller, R. M. Melant, and C. F. Zukoski, "Comparison of the Compressive Yield Response of Aggregated Suspensions: Pressure Filtration, Centrifugation, and Osmotic Consolidation," *J. Am. Ceram. Soc.*, **79** [10] 2545–56 (1996).

[5] A. C. Young. O. O. Omatete, M. A. Janney, and P. A. Menchhofer, "Gelcasting of Alumina," *J. Am. Ceram. Soc.*, **74** [3] 612–18 (1991).

[6] S. L. Morissette and J. A. Lewis, "Chemorheology of Aqueous Alumina–Poly(vinyl alcohol) Gelcasting Suspensions," *J. Am. Ceram. Soc.*, **82** [3] 521–28 (1999).

[7] T. J. Graule, W. Si, F. H. Baader, and L. J. Gaukler, "Direct Coagulation Casting (DCC): Fundamentals of a New Forming Process for Ceramics"; pp. 457–61 in Ceramic Transactions, Vol. 51, *Ceramic Processing Science and Technology*. Edited by H. Hausner, G. L. Messing, and S. Hirano. American Ceramic Society, Westerville, OH, 1995.

[8] J. Cesarano III and T. A. Bear, "Recent Developments in Freeform Fabrication of Dense Ceramics from Slurry Deposition"; pp. 25–32 in *Proceedings of the Solid Freeform Fabrication Symposium* (Austin, TX). Edited by J. J. Beaman, D. L. Bourell, R. H. Crawford, H. L. Marcus, and J. W. Barlow. University of Texas, Austin, TX, 1997.

[9] T. K. Garino and H. K. Bowen, "Kinetics of Constrained-Film Sintering," *J. Am. Ceram. Soc.*, **73** [2] 251–57 (1990).

[10] G. W. Scherer, "Drying Gels, VIII. Revision and Review," *J. Non-Cryst. Solids*, **109**, 171–82 (1989).

[11] G. W. Scherer, "Physics of Drying"; pp. 179–97 in *Ultrastructure Processing of Advanced Material.* Edited by D. R. Uhlmann and D. R. Ulrich. Wiley, New York, 1992.

[12] M. Descamps, M. Mascart, and B. Thierry, "How to Control Cracking of Tape-Cast Sheets," *Am. Ceram. Soc. Bull.*, **74** [3] 89–92 (1995).

[13] E. Streicher and T. Chartier, "Study of Cracking and Microstructural Evolution during Drying of Tape-Cast Aluminum Nitride Sheets," *J. Mater. Sci.*, **26**, 1659–65 (1991).

[14] R. C. Chiu and M. J. Cima, "Drying of Granular Ceramic Films: I, Effects of Processing Variables on Cracking Behavior," *J. Am. Ceram. Soc.*, **76** [9] 2257–64 (1993).

[15] R. C. Chiu and M. J. Cima, "Drying of Granular Ceramic Films: II, Drying Stress and Saturation Uniformity," *J. Am. Ceram. Soc.*, **76** [11] 2769–77 (1993).

[16] J. A. Lewis, K. A. Blackman, A. L. Ogden, J. A. Payne, and L. F. Francis, "Rheological Properties and Stress Development during Drying of Tape-Cast Ceramic Layers," *J. Am. Ceram. Soc.*, **79** [12] 3225–34 (1996).

[17] G. E. Anner, *Planar Processing Primer*; pp. 439–91. Van Nostrand Reinhold, New York, 1995.

[18] D. M. Smith, G. W. Scherer, and J. M. Anderson, "Shrinkage during Drying of Silica Gel," *J. Non-Cryst. Solids*, **188**, 191–206 (1995).

[19] R. Buscall, "The Sedimentation of Concentrated Colloidal Suspensions," *Colloids Surf.*, **43**, 33–53 (1990).

[20] R. Buscall and L. R. White, "The Consolidation of Concentrated Suspensions, Part I—The Theory of Sedimentation," *J. Chem. Soc. Faraday Trans. 1*, **83**, 873–91 (1987).

[21] R. Buscall, P. D. A. Mills, J. W. Goodwin, and D. W. Lawson, "Scaling Behavior of the Rheology of Aggregate Networks Formed from Colloidal Particles," *J. Chem. Soc. Faraday Trans. 1*, **84** [12] 42–49 (1988).

[22] K. A. Landman and L. R. White, "Solid/Liquid Separation of Flocculated Suspensions," *Adv. Colloid Interface Sci.*, **51**, 175–246 (1994).

[23] K. T. Miller, W. Shi, L. J. Struble, and C. F. Zukoski, "Compressive Yield Stress of Cement Paste," *Mater. Res. Soc. Symp. Proc.*, **370**, 285–91 (1995).

[24] W. Shih, S. I. Kim, W. Y. Shih, C. H. Schilling, and I. A. Aksay, "Consolidation of Colloidal Suspensions," *Mater. Res. Soc. Symp. Proc.*, **180**, 167–72 (1990).

[25] W. Shih, W. Y. Shih, S. Kim, and I. A. Aksay, "Equilibrium-State Density Profiles of Centrifuged Cakes," *J. Am. Ceram. Soc.*, **77** [2] 540–46 (1994).

[26] G. M. Channell and C. F. Zukoski, "Shear and Compressive Rheology of Aggregated Alumina Suspensions" *AIChE J.*, **43** [7] 1700–708 (1997).

[27] R. Buscall, "The Elastic Properties of Structured Dispersions: A Simple Centrifuge Method of Examination," *Colloids Surg.*, **5**, 269–83 (1982).

[28] G. G. Stoney, "The Tension of Metallic Films Deposited by Electrolysis," *Proc. R. Soc. London*, **A82**, 172 (1909).

[29] G. W. Scherer, "Fundamentals of Drying and Shrinkage"; pp. 199–211 in *Science of Whitewares.* Edited by V. E. Henkes, G. Y. Onoda, and W. M. Carty. American Ceramic Society, Westerville, OH, 1997.

[30] T. M. Shaw, "Drying as an Immiscible Displacement Process with Fluid Counterflow," *Phys. Rev. Lett.*, **59** [15] 1671–74 (1987).

[31] F. M. Auzerais, R. Jackson, and W. B. Russel, "The Resolution of Shocks and the Effects of Compressive Sediments in Transient Settling," *J. Fluid Mech.*, **195**, 437–62 (1988).

[32] N. F. Carnahan and K. E. Starling, "Equation of State for Nonattracting Rigid Spheres," *J. Chem. Phys.*, **51** [2] 635–36 (1969).

[33] C. Allain, M. Cloitre, and M. Wafra, "Aggregation and Sedimentation in Colloidal Suspensions," *Phys. Rev. Lett.*, **74** [8] 1478–81 (1995).

[34] J. Guo, "Aggregation Effects on the Rheological, Sedimentation, and Drying Behavior of Colloidal Silica Suspensions"; Ph.D. Thesis. University of Illinois, Urbana, IL, 1997.

[35] M. J. Cima, J. A. Lewis, and A. D. Devoe, "Binder Distribution Processes in Ceramic Greenware during Thermolysis," *J. Am. Ceram. Soc.*, **72** [7] 1192–99 (1989).

[36] R. D. Deegan, O. Bakajin, T. F. Dupont, G. Huber, S. R. Nagel, and T. A. Witten, "Capillary Flow as the Cause of Ring Stains from Dried Liquid Drops," *Nature (London)*, **389**, 827–29 (1997). □